

Behrends, Gert ; Stöbener, Dirk ; Fischer, Andreas

### Lateral scanning white-light interferometry on rotating objects

Journal Article as: peer-reviewed accepted version (Postprint)

DOI of this document\* (secondary publication): <https://doi.org/10.26092/elib/3324>

Publication date of this document: 20/09/2024

\* for better findability or for reliable citation

#### Recommended Citation (primary publication/Version of Record) incl. DOI:

Gert Behrens and Dirk Stöbener and Andreas Fischer. Lateral scanning white-light interferometry on rotating objects. 2020. In: Surface Topography: Metrology and Properties, 8 (3), 035006, <https://dx.doi.org/10.1088/2051-672X/aba484>

Please note that the version of this document may differ from the final published version (Version of Record/primary publication) in terms of copy-editing, pagination, publication date and DOI. Please cite the version that you actually used. Before citing, you are also advised to check the publisher's website for any subsequent corrections or retractions (see also <https://retractionwatch.com/>).

This is the Accepted Manuscript version of an article accepted for publication in Measurement Science and Technology. IOP Publishing Ltd is not responsible for any errors or omissions in this version of the manuscript or any version derived from it. The Version of Record is available online at <https://dx.doi.org/10.1088/2051-672X/aba484>

This document is made available under a Creative Commons licence.




The license information is available online: <https://creativecommons.org/licenses/by-nc-nd/4.0/>

#### Take down policy

If you believe that this document or any material on this site infringes copyright, please contact [publizieren@suub.uni-bremen.de](mailto:publizieren@suub.uni-bremen.de) with full details and we will remove access to the material.

## PAPER

# Lateral scanning white-light interferometry on rotating objects

Gert Behrends<sup>1</sup> , Dirk Stöbener<sup>1,2</sup>  and Andreas Fischer<sup>1,2</sup> 

<sup>1</sup> University of Bremen, Bremen Institute for Metrology, Automation and Quality Science, Bremen, Germany

<sup>2</sup> University of Bremen, MAPEX Center for Materials and Processes, Bremen, Germany

E-mail: [g.behrends@bimaq.de](mailto:g.behrends@bimaq.de)

**Keywords:** white-light interferometry, topography, curvature, rotation

---

## Abstract

White-light interferometry (WLI) has been widely established as a contact-free measurement method for surface topographies. While the widespread vertical scanning approach provides a height resolution of under 1 nm, it is not suitable for measurements on objects in motion. An alternative for moving surfaces is laterally scanning white-light interferometry (LSWLI). Though LSWLI allows to measure objects in motion, the measurement on rotating, curved objects is still challenging, since the tilt angle between the optical axis of the WLI and the surface normal varies over the field of view, and the height evaluation strongly depends on the tilt angle that needs to be calibrated. For this reason, an enhancement of the signal evaluation is proposed that enables LSWLI measurements on rotating objects, cylinders in particular, without a preceding calibration of the tilt angle distribution in the field of view. This was achieved by enhancing a self-calibration algorithm originally developed for linearly scanned, plane surfaces with spatially resolved time-frequency analysis. Using this self-calibrating algorithm, the local tangent surface angles present in the field of view of the LSWLI are retrieved and used to calculate the micro topography of a cylindrical specimen. These topography data contain no information on the global shape of the object, therefore shape-removal algorithms, as needed for VSWLI measurements, are not necessary. As a byproduct of the angle evaluation, the radius of the cylindrical specimen can be determined in addition. The comparison with VSWLI reference data finally shows that the LSWLI setup is able to produce similar topography results despite the much inferior hardware.

---

## 1. Introduction

### 1.1. Motivation

Rising demands regarding the quality of optically smooth surfaces of consumer goods and industrial intermediate products necessitate metrology that is able to quantify the topography of these surfaces in a quick and accurate manner. Systems capable of in-process measurements are especially interesting for manufacturers, as early detection of defects reduces production costs [1, 2].

For delicate surfaces, such as optical components or highly reflective functional and decorative surfaces, a contactless measurement method is desired. Therefore, the measurement approach should be based on an optical measurement principle. In addition, the method's accuracy should be in the single-digit nanometer range to resolve the surface roughness, i.e. shape deviations of the third order and above [3].

Furthermore, the surfaces of interest are often not plane, but curved surfaces of revolution. It is impractical to create calibration objects, which accurately represent the measurement objects' geometry (i.e. curvature), for every thinkable measurement task. Hence, an optical surface measurement technique is required, which is capable of measuring on rotating, curved surfaces of revolution with nanometer resolution and with the ability to adapt to varying surface curvatures without external calibration aides.

### 1.2. State of the Art

A widespread optical technique, which is able to provide areal surface topography measurements with height resolutions  $< 1$  nm, is white-light interferometry (WLI). It is specified in DIN EN ISO 25178, where it is referred to as coherence scanning interferometry (CSI) [4]. A common variation is the vertically scanning WLI (VSWLI), where the term 'vertical'

means the direction of the optical axis. The term ‘white-light interferometry’ can be traced back to Flournoy *et al*, who used it for film thickness gauging since the 1970s [5]. Its modern, digitally imaging form was first described in principle by Davidson *et al* in 1987 (as ‘coherence probe microscope’) [6] and as a tool for profilometry by Lee and Strand in 1990 (as ‘coherence scanning microscope’) [7]. Kino and Chim were first to use a Mirau-type interferometer setup, as is used in the experiments for this article, in 1990 (as ‘Mirau correlation microscope’) [8]. Further insights into this now widespread technique can be found in these review papers [9, 10].

The application of VSWLI on non-planar surfaces has been investigated both theoretically and experimentally. Lehmann [11] theoretically investigated chromatic aberrations occurring in VSWLI on curved surfaces. The practical application of VSWLI on a hemispheric surface has been investigated by Riebeling *et al* [12]. The influence of tilt and curvature of spheres on scanning white-light interferometry has been investigated by Su *et al* [13]. Scheiding *et al* [14] used WLI to measure microoptical lens arrays. They all demonstrated that VSWLI can also be used on curved surfaces. However, VSWLI on continuously moving surfaces is problematic, because the setup requires the measurement object to not move laterally during the vertical scan.

For this reason, laterally scanning white-light interferometry (LSWLI) was developed by Olszak in 2000 [15], which allows to perform measurements on moving surfaces. LSWLI combines the usually separated vertical (for height measurement) and horizontal (for areal measurements) scanning movements in one scan path. This is realized by moving the measurement object on a tilted scan path through the interferometer’s measurement volume, i.e. the tilt angle between the surface normal and the optical axis is non-zero. For this lateral scanning method, the measured heights of the surface topography are calculated based on the tilt angle. Therefore, knowledge of the tilt angle is a necessity.

The tilt angle can be adjusted prior to the measurement by using a plane calibration object such as a mirror. This can be a time consuming, tedious task. Therefore, Munteanu [16] developed a self-calibration method for plane surfaces, which allows the calculation of the tilt angle from the fringe frequencies in the raw data and parameters of the illumination and the camera sensor.

When applying LSWLI on rotating, curved surfaces of revolution, however, finding the correct angle for the height calculation becomes more complicated. There is not one distinct tilt angle, like on a translationally moved, plane surface, but a range of local tangent angles to the surface according to the curvature of the surface and its circular, rotatory scan path, see figure 1.

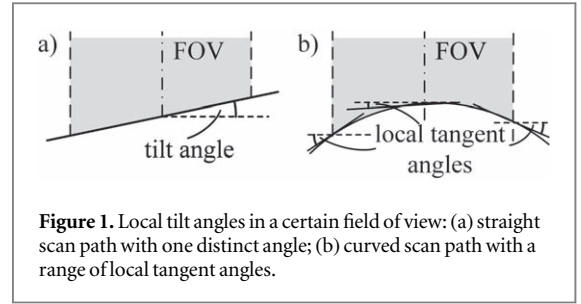


**Figure 1.** Local tilt angles in a certain field of view: (a) straight scan path with one distinct angle; (b) curved scan path with a range of local tangent angles.

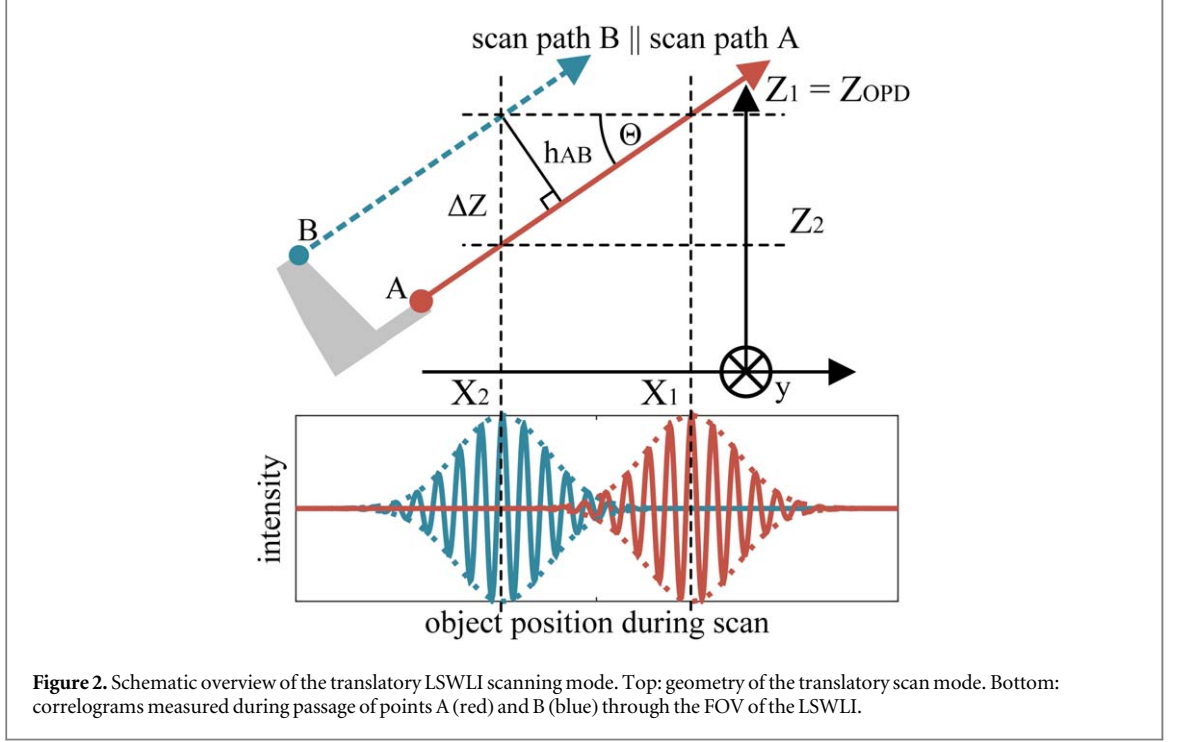
Finding these angles using a calibration object would require an object, which closely resembles the geometry of the measurement object. This procedure is inflexible, as there would have to be a calibration object with a fitting curvature for every object the LSWLI is supposed to be applied on.

Instead of using a calibration object, Bahr, Domaschke *et al* [17, 18], used laser triangulation to firstly digitize the shape of their rotationally symmetric measurement objects and then guide a robot-mounted LSWLI on the associated, pre-calculated scan path. However, this calibration approach requires a more complex hardware setup and time to digitize the object shape prior to the actual surface measurement, which limits its use for in-process applications. In summary, an LSWLI-based measurement approach that is applicable on rotating, curved surfaces without the need of a specific calibration object or a preceding measurement of the object shape is missing.

### 1.3. Aim and outline

For this reason, the aim of the article is to present a LSWLI scanning mode for rotating, curved surfaces that makes use of an enhancement of Munteanu’s method for curved surfaces. This allows areal LSWLI measurements on a rotating cylindrical object without prior calibration of the locally varying tangent angle. Note that the proposed method is applicable for any surface of revolution, but is demonstrated here on the example of a cylindrical object, as one long-term goal is to apply the measurement system for in-process inspection of sheet metal working rolls.

In section 2 the principle of rotatory LSWLI is introduced as a modification of translatory LSWLI to measure on a rotating object. The rotatory LSWLI makes use of Munteanu’s method, which was extended for curved scan paths. Furthermore, the geometrical conditions are outlined under which rotatory LSWLI is able to operate. The experimental setup is described in section 3, and the results, which validate the theoretical findings, are presented and discussed in section 4. The validation includes a comparison with reference measurements using conventional VSWLI. The article closes with a summary and an outlook.



## 2. Modes of scanning white-light interferometry

After reintroducing the general principles of scanning WLI, including the VSWLI and translatable LSWLI approaches in section 2.1, the enhanced rotatory LSWLI scanning mode is described in section 2.2. The range of acceptable surface tangent angles and the resulting usable measurement positions on a cylinder are finally derived in section 2.3.

### 2.1. Measurement principle of scanning WLI

The general principle for scanning white-light interferometry devices follows the setup of a Michelson interferometer. The Mirau type setups work in a similar fashion with the exception that their reference path is paraxial to the measurement path. The detected signal intensity depends on the optical path length difference (OPD), which is the difference between the lengths of the reference path  $l_{\text{ref}}$  and the measurement path  $l$ . The intensity of the observed signal alternates between constructive and destructive interference if the length of the measurement path is changed continuously in a certain range (cf figure 2, lower part). The so called correlogram's intensity and also the interference contrast between a maximum and its adjacent minima in the correlogram are maximal for the surface position  $z = z_{\text{OPD}}$ , where  $l - l_{\text{ref}} = 0$ .

With VSWLI the position  $z_{\text{OPD}}$  is determined for each pixel of the field of view (FOV) individually by a surface scan in  $z$ -direction.  $z_{\text{OPD}}$  equals the  $z$ -position, where the envelope of the recorded intensity reaches its maximum. The height coordinate  $h_i$  of a surface point  $i$  corresponds to the scan position  $z_{\text{OPD},i}$  and as a result, the height difference  $h_{ij}$  between two surface

points  $i$  and  $j$  is obtained by evaluating the difference of the two scan positions  $h_{ij} = z_{\text{OPD},i} - z_{\text{OPD},j}$ .

In translatable LSWLI an object is moved laterally through the FOV on a tilted scan path. Due to the tilt angle  $\Theta$  of the scan path, each surface point of the object not only moves horizontally ( $x$ -direction) through the FOV, but also in vertical direction ( $z$ -direction), cf figure 2. This change in vertical position corresponds to a  $z$ -scan and results in a correlogram comparable to the ones shown at the bottom of figure 2 accordingly. The two surface points A and B have a height difference of  $h_{AB}$  in the surface coordinate system. Point A moves through the FOV on scan path A (solid red line) and intersects the  $z_{\text{OPD}}$ -line at  $x_1$ . Point B moves through the FOV on scan path B (dotted blue line), which is parallel to scan path A and vertically shifted by  $\Delta z = z_1 - z_2$ . Point B intersects the  $z_{\text{OPD}}$ -line at  $x_2$ . The vertical distance  $\Delta z = (x_2) \cdot \tan(\Theta)$  between the scan paths can be converted to the actual surface height difference  $h_{AB}$  by evaluating the cosine of the tilt angle  $\Theta$ :

$$h_{AB} = \Delta z \cdot \cos(\Theta) = (x_1 - x_2) \cdot \sin(\Theta). \quad (1)$$

As a result, the height difference between two arbitrary surface points A and B can be calculated from the tilt angle of the scan paths and the  $x$ -positions, at which the envelopes of their correlograms become maximal.

The positions  $x_1$  and  $x_2$  are known from the controlled surface movement and the evaluation of the corresponding correlograms. For ease of calculation, a reference position  $x_1$  is assigned to a pixel of the camera sensor in scan direction.

As a digital camera in the  $x$ - $y$ -plane is used to record the signals, a continuous stream of surface

points is observed moving through the FOV in horizontal  $x$ -direction (line measurement). Depending on the number of camera pixels in  $y$ -direction, multiple rows of points are recorded in parallel (areal measurement).

According to equation (1), the tilt angle of the scan path needs to be known, which is either obtained from a calibration with a reference object or the self-calibration method developed by Munteanu [16]. Munteanu's method uses the frequency  $f_{\text{corr}}$  of the intensity fringes in the correlograms to calculate the tilt angle of the scanning path:

$$|\Theta| = \arctan\left(\frac{f_{\text{corr}} \lambda_0}{2 s_{\text{pixel}} N_{\text{pixel},x}}\right), \quad (2)$$

where  $\lambda_0$  is the central wavelength of the illumination,  $s_{\text{pixel}}$  is the width of the surface observed by a pixel and  $N_{\text{pixel},x}$  is the number of pixels in scan direction, over which the frequency is evaluated.

While translatory LSWLI works well for plane objects, it is impractical for measurements on surfaces of revolution, such as cylinders. As the measurement volume of a LSWLI is usually much smaller in axial direction than the object to be measured, it would require a multitude of translatory scans, passing tangentially over a fraction of the object's surface after each incremental rotation of the object. This negates the advantages of LSWLI over VSWLI, namely the ability to measure during continuous movement without stitching.

## 2.2. Measurement principle of rotatory LSWLI

The difference between the classical, translatory LSWLI method and rotatory LSWLI lies in the different scanning motion. Due to the rotational movement of the measurement object the object's surface moves on a curved scan path. Mounting the WLI optics at a fixed position relative to the measurement object allows LSWLI for rotatory movements. The challenge of this setup is, however, that the sampling steps in  $z$ -direction are not equidistant due to the curved scan path of each surface element. Each step depends on the lateral position of the surface element in the FOV and the measurement position over the surface profile.

The rotatory scan mode is illustrated in figure 3. The surface points A and B move on the concentric, circular scan paths A (solid red line) and B (dotted blue line) around the coordinate origin. Note that the radius of scan path B is larger than the radius  $r$  of scan path A by the structure height  $h_{\text{AB}}$ , which is the measurand. Points A and B intersect the  $z_{\text{OPD}}$ -line at the  $x$ -coordinates  $x_1$  and  $x_2$ , respectively. While passing through the FOV of the LSWLI, the correlograms at the bottom of the figure can be observed for the points A and B. As the  $z$ -coordinate change on the curved scan paths is not linear, the frequencies of the

correlograms decrease with proximity to the apex of the scan path.

According to the illustrated geometry, a system of four equations is considered to derive the structure height  $h_{\text{AB}}$  as a function of the positions  $x_1$ ,  $x_2$  and the tangent angles  $\Theta_1$ ,  $\Theta_2$ :

$$\Delta z = z_1 - z_2 = r \cdot (\cos(\Theta_1) - \cos(\Theta_2)), \quad (3.1)$$

$$\Delta z = (x_1 - x_2) \cdot \tan\left(\frac{\Theta_1 + \Theta_2}{2}\right), \quad (3.2)$$

$$r \cdot \sin(\Theta_2) = (r + h_{\text{AB}}) \cdot \sin(\xi), \quad (3.3)$$

$$r \cdot \cos(\Theta_1) = (r + h_{\text{AB}}) \cdot \cos(\xi), \quad (3.4)$$

Equation (3.1) describes the vertical difference  $z_1 - z_2$  using the parametric circle equation for scan path A. Equation (3.2) describes the vertical difference  $z_1 - z_2$  using the horizontal distance  $x_1 - x_2$  and the angle of the chord connecting both positions on scan path A. Equation (3.3) is the equality of the coordinate  $x_2$  for the respective points on both scan paths A and B (using again the parametric circle equations), as does equation (3.4) for the common coordinate  $z_1$ . The unknown radius  $r$  can be expressed with  $x_1$ ,  $x_2$ ,  $\Theta_1$  and  $\Theta_2$  by solving equation (3.1) = equation (3.2). The unknown tangent angle  $\xi$  as an expression of  $\Theta_1$  and  $\Theta_2$  is obtained by reforming (3.3) and (3.4) for  $h_{\text{AB}}$  and then equating both expressions to get  $\xi$ . The expressions for  $r$  and  $\xi$  are then applied to either (3.3) or (3.4) and solved for  $h_{\text{AB}}$ :

$$h_{\text{AB}} = \frac{(x_1 - x_2) \tan\left(\frac{\Theta_1 + \Theta_2}{2}\right)}{\cos(\Theta_1) - \cos(\Theta_2)} \cdot \left(\cos(\Theta_1) \sqrt{\frac{\sin^2(\Theta_2)}{\cos^2(\Theta_1)} + 1} - 1\right). \quad (4)$$

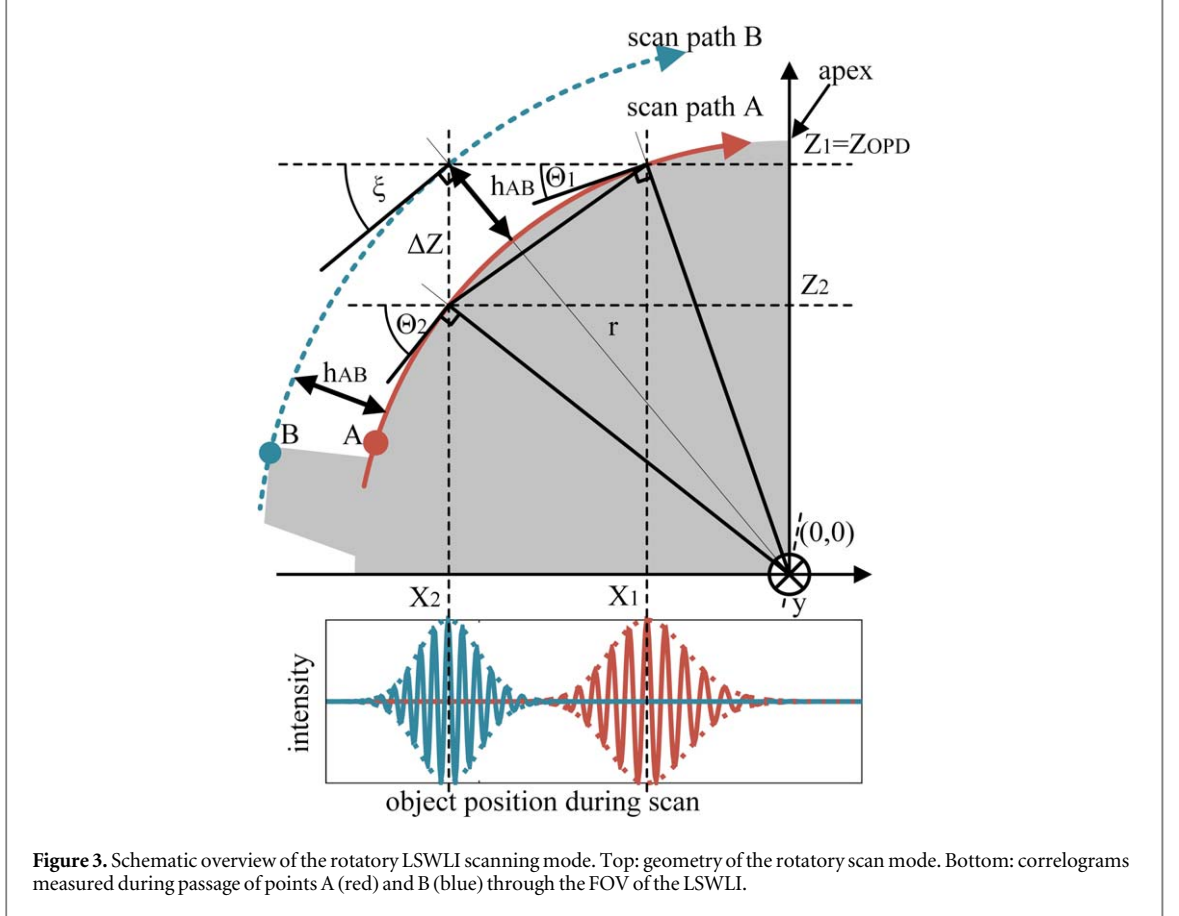
This equation for  $h_{\text{AB}}$  relies on the tangent angles  $\Theta_1$ ,  $\Theta_2$  on scan path A and the horizontal coordinates  $x_1$  and  $x_2$ , which mark the positions at which the correlograms' envelopes of points A and B are maximal. All of these quantities can be retrieved from the LSWLI recording.

In contrast to translatory LSWLI, where only the tilt angle is characteristic for the scanning procedure, the scan path of rotatory LSWLI is circular so that the local tangent angle of the scan path, which changes during rotation through the FOV, is decisive for the correlogram generation. In the correlograms this is observable as a change of the fringe frequency (cf figure 3). In order to apply Munteanu's self-calibration approach to determine the tangent angle, equation (2) has to be enhanced by spatially resolved frequency analysis to yield the respective local tangent angles  $\Theta(x)$ :

$$|\Theta(x)| = \arctan\left(\frac{f_{\text{corr}}(x) \lambda_0}{2 s_{\text{pixel}} N_{\text{pixel},x}}\right), \quad (5)$$

where  $f_{\text{corr}}(x)$  is the local frequency of the fringes in the correlogram,  $\lambda_0$  is the central wavelength of the





illumination,  $s_{\text{pixel}}$  is the width of the magnified pixel and  $N_{\text{pixel},x}$  is the number of pixels in scan direction, over which the frequency is evaluated. Note that the equation gives an absolute value of the angle. If the FOV spanned over the apex of the scan path, a priori knowledge of the change of the angle's sign would have to be taken into account.

As a result, the LSWLI measurement principle is enhanced for a rotary scanning mode. The translatory mode is included as a special case of the rotatory scanning mode, cf equation (1) with equation (4) for  $\Theta_1 = \Theta_2 = \Theta$ , where the scan paths have infinitely large radii, and thus appear as straight paths in the FOV with a common tilt angle.

### 2.3. Measurement window of rotatory LSWLI

The measurement window (measurement range and resolution) of LSWLI, rotatory LSWLI in particular, strongly depends on the (local) tangent angles of the scan paths with respect to the WLI's optical axis. A steeper angle results in a larger axial measurement range. If a specific range is required to capture the complete topography of the object, a certain minimal tangent angle is required. At the same time, a steeper angle also results in a coarser sampling. This in turn means a measurement with a certain resolution can only be carried out up to a certain maximal tangent angle. Finding the best compromise between range and resolution is especially challenging for rotatory LSWLI due to the curvature of the scan path. Thus, the

limits of the measurement window are established in the following geometric considerations for cylindrical objects.

#### 2.3.1. Measurement range requirement

In order to measure a specific range of structure heights  $h_{AB}$  the FOV edge has to be positioned at a certain minimal distance  $x_{\text{min}}$  to the apex. The tangent angle at this position is  $\Theta_{\text{min}}$ .

The x-coordinates of the FOV edges on a scan path thus read (using the parametric circle equation)  $x_{\text{min}} = r \sin(\Theta_{\text{min}})$  and  $x_{\text{min}} - w = r \sin(\Theta_2)$ , where  $r$  is the scan path radius,  $x_{\text{min}}$  is the distance between the scan path apex and the beginning FOV edge and  $w$  is the FOV width, cf figure 4. Using these coordinates of the FOV in conjunction with equation (4) allows calculating the minimal tangent angle depending on the workpiece structure heights  $h_{AB}$ :

$$\Theta_{\text{min},h_{AB}} = \arcsin\left(\frac{h_{AB}^2 + 2h_{AB}r - w^2}{2r w}\right). \quad (6)$$

For large radii, the angle  $\Theta_{\text{min},h_{AB}}$  asymptotically becomes  $\arcsin(h_{AB}/w)$ . Under the condition that only angles in the range  $0^\circ < \Theta < 90^\circ$  are allowed, this limit has the same form as the constant angle present in translatory LSWLI.

As the interferometer does not directly measure  $h_{AB}$ , but the vertical projection  $\Delta z$  of the structure, there is a further limitation to the minimal tangent

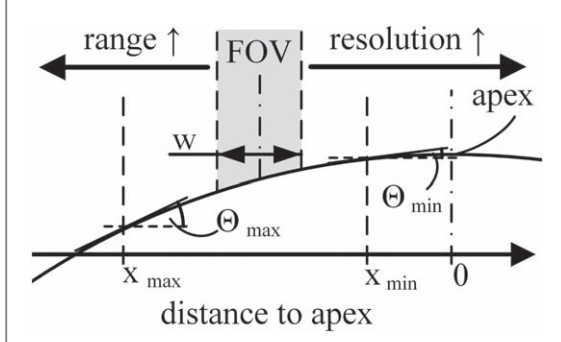


**Figure 4.** Position of the FOV in relation to the curved scan path and the distance to apex. The measurement window is located between  $x_{\min}$  and  $x_{\max}$ . The FOV is assumed smaller than the measurement window. Measuring closer to the apex yields finer resolution, but smaller measurement range.

angle from the signal's point of view. It is assumed that the signal is only evaluable, if the correlogram decays by at least 50% throughout the FOV. Therefore, a lower bound of  $\Theta_{\min, \Delta z}$  is given by the condition  $\Delta z = l_c$ , with  $l_c$  as the FWHM coherence length. Applying this condition and the  $x$ -coordinates of the FOV on equation (3.1) yields

$$\Theta_{\min, \Delta z} = \arcsin\left(\frac{l_c}{2r} \sqrt{\frac{4r^2}{l_c^2 + w^2} - 1} - \frac{w}{2r}\right). \quad (7)$$

The lower bound for the tangent angle at large radii is  $\arcsin(l_c (l_c^2 + w^2)^{-1/2})$ . To take measurements at tangent angles of the surface below this bound, additional tilting of the optics with respect to the scan path (like it is done for the translatory case) is necessary, as the height change due to the curvature is not sufficient.

The minimum tangent angle therefore depends on both workpiece-specific and measuring system-specific parameters, so that for a particular measuring task the larger of the two limit values must be used to define the measurement window.

### 2.3.2. Axial measurement resolution requirement

In order to achieve a certain minimal physical resolution  $\Delta h_{AB}$  for the structure height, the far end of the FOV can at most have a distance to the apex of  $x_{\max}$ . The axial resolution depends on the accuracy of the algorithm responsible for the evaluation of the recorded correlograms. To assess the axial resolution independently of an algorithm, the actual physical distance of the observing pixels is used as a figure of merit. The physical resolution is here defined as the structure height difference  $\Delta h_{AB}$  that can be observed by the last two neighbouring pixels of the FOV  $x_{\max} + s_{\text{pixel}}$  and  $x_{\max}$ , where  $s_{\text{pixel}}$  is the distance between two surface points observed by neighbouring pixels. Analogous to  $\Theta_{\min, h_{AB}}$ , a maximal tangent angle  $\Theta_{\max, \Delta h_{AB}}$ , is obtained from equation (4):

$$\Theta_{\max, \Delta h_{AB}} = \arcsin\left(\frac{\Delta h_{AB}^2 + 2\Delta h_{AB} r - s_{\text{pixel}}^2}{2r s_{\text{pixel}}}\right). \quad (8)$$

For large radii, the angle  $\Theta_{\max, \Delta h_{AB}}$  approaches the limit  $\arcsin(\Delta h_{AB}/s_{\text{pixel}})$ , which is the same as for the translatory scan mode. For a LSWLI with a fixed pixel size, the physical measurement resolution requirement for an object with a certain nominal radius can be fulfilled at measurement positions with surface tangent angles of at most  $\Theta_{\max, \Delta h_{AB}}$ .

From the signal's point of view the maximal observable vertical distance between two pixels is  $\Delta z = \lambda_{\text{eff}}/2$ . It uses the effective wavelength  $\lambda_{\text{eff}} = f(\lambda_0, NA)$ , where  $NA$  is the numerical aperture.  $\Delta z$  is a figure of merit for the spacing between a constructive and destructive interference fringe (phase change of  $\pi$ ). Using this condition and the  $x$ -coordinates of the last two pixels in the FOV on equation (3.1) results in

$$\Theta_{\max, \Delta z} = \arcsin\left(\frac{\lambda_{\text{eff}}}{4r} \sqrt{\frac{4r^2}{\frac{\lambda_{\text{eff}}^2}{4} + s_{\text{pixel}}^2} - 1} - \frac{s_{\text{pixel}}}{2r}\right). \quad (9)$$

For large radii, the angle  $\Theta_{\max, \Delta z}$  approaches the limit  $\arcsin(\lambda_{\text{eff}}/2 (\lambda_{\text{eff}}^2/4 + s_{\text{pixel}}^2)^{-1/2})$ . Applying the Rayleigh criterion for the smallest usable pixel spacing  $s_{\text{pixel}} = \Delta x_{\text{Rayleigh}} = 1.22\lambda_0 NA^{-1}$  on the limit results in  $\Theta_{\max, \Delta z} = \arctan(2.44^{-1} NA \lambda_{\text{eff}} \lambda_0^{-1})$ , which equals the critical angle for measurability for white-light interferometry described by Lehmann *et al* [19].

Accordingly, also the maximum tangent angle is determined by workpiece-specific and measuring system-specific parameters and the lower angle value has to be chosen for the measurement window.

## 3. Experimental setup

The rotatory scanning mode introduced in section 2.2 is validated experimentally. The setup used is outlined in section 3.1 and the recording and evaluation process is described in section 3.2. The measuring positions, which can be used with the setup according to section 2.3, are studied in section 3.3.

### 3.1. Setup

The rotatory LSWLI setup consists of a typical laterally scanning white light interferometer (cf [15]) and a rotation stage with the specimen. The interferometric setup is mounted horizontally on a pneumatically damped optical bench. The rotation stage for the movement of the specimen is placed in front of the objective. The LSWLI's focus and the specimen's lateral position, eccentricity and wobble can be adjusted manually. Schematic and photography of this setup are shown in figure 5.

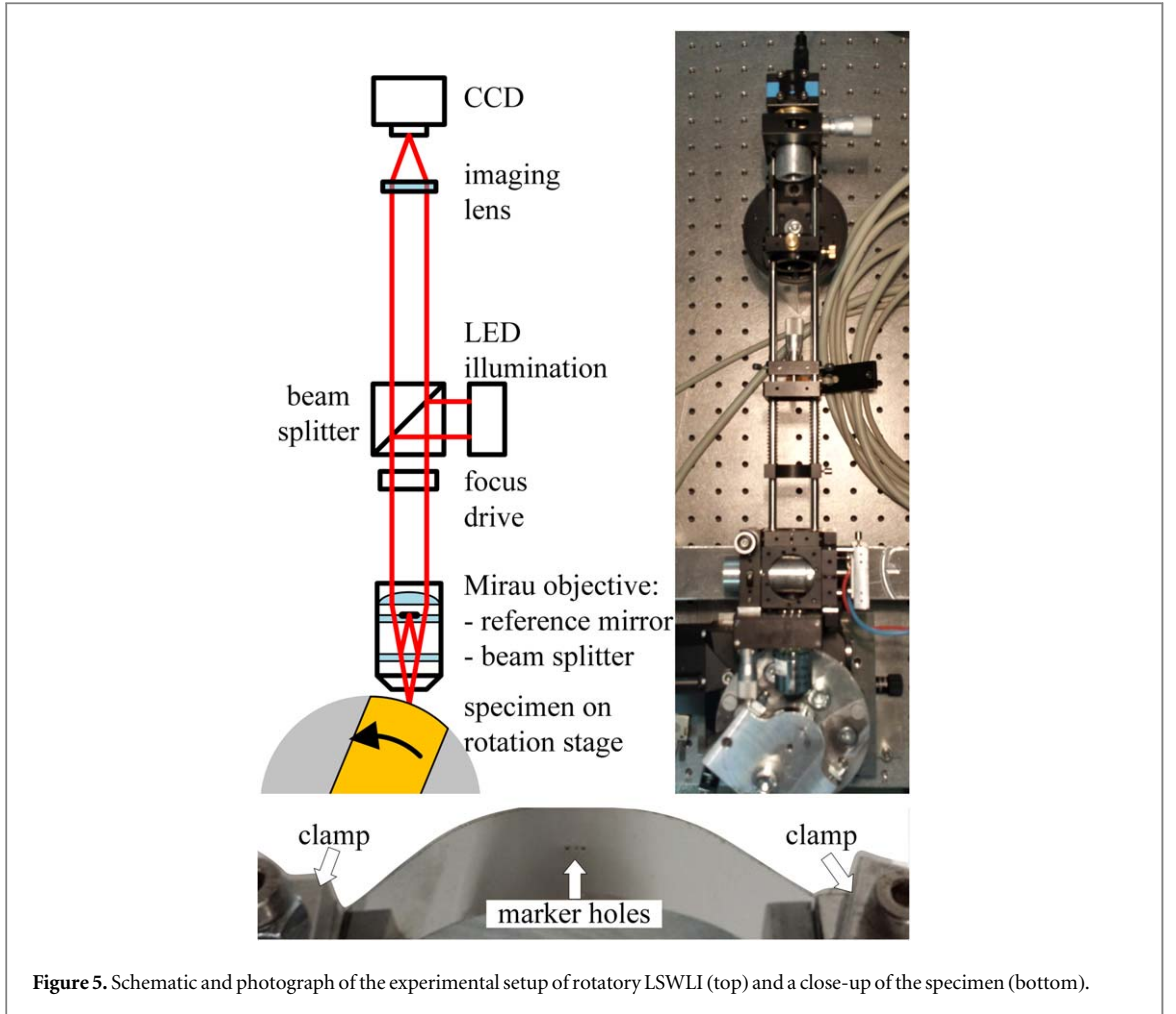


Figure 5. Schematic and photograph of the experimental setup of rotatory LSWLI (top) and a close-up of the specimen (bottom).

Table 1. Properties of the hardware used for the LSWLI.

CCD camera			
resolution (ROI)	bit depth	pixel size	
$640 \times 480$ pixel	8 bit	$6 \mu\text{m}$	
Mirau Objective			
magnification	NA	FOV size	Depth of field
$10\times$	0.3	$384 \times 288 \mu\text{m}^2$	$7.88 \mu\text{m}$
LED			
central wavelength $\lambda_0$	FWHM bandwidth $\Delta\lambda$	coherence length $l_c$	
530 nm	70 nm	$3.54 \mu\text{m}$	

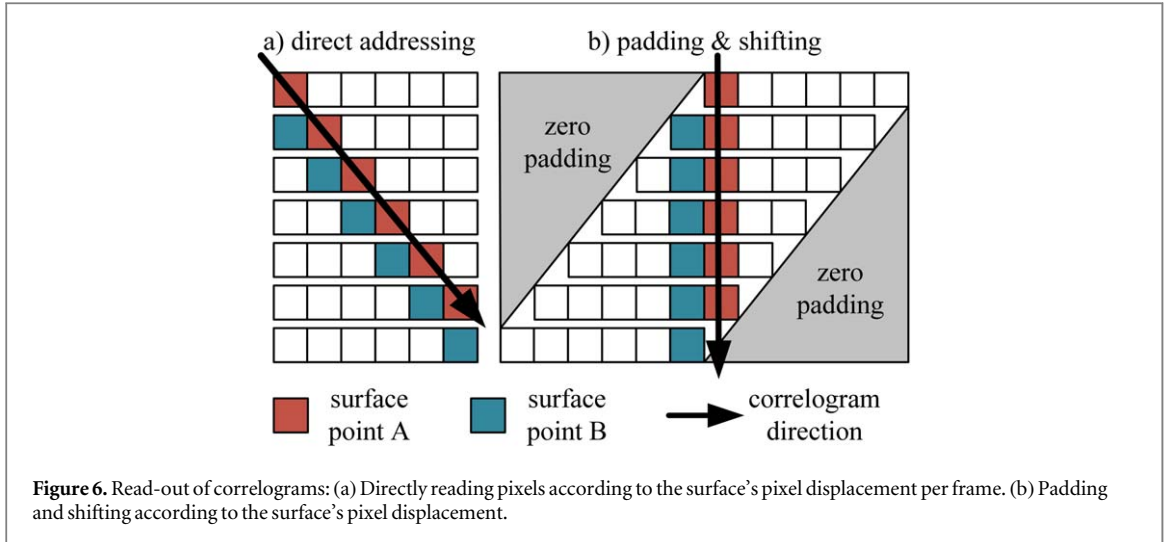
The properties of the principal components of the LSWLI system are listed in table 1. This prototype mainly consists of a digital camera (The Imaging Source DMK 22BUC03) with  $1/3''$  CCD sensor, which is chosen because of its global shutter and trigger input. A Nikon  $10\times/0.3$  Mirau Objective is used to achieve a project-specified lateral resolution and a 530 nm LED provides a spectrum comparable to those used in commercial WLIs. The body of the WLI optics consists of Qioptiq microbank components. The total magnification of the system (objective, body, imaging

lens) is determined to  $10.29\times$ . This means, that each  $(6 \mu\text{m})^2$  pixel of the camera sees a surface of  $(0.583 \mu\text{m})^2$  area. The resulting area of the FOV for this setup has a width of  $373.12 \mu\text{m}$  in scan direction.

The VSWLI system used for reference measurements is a GBS smartWLI compact equipped with a 2.3 MP camera and a  $20\times/0.4$  Mirau objective, resulting in a FOV of  $0.91 \times 0.58 \text{ mm}^2$  with a point spacing of  $0.48 \mu\text{m}$ .

The specimen is also shown in figure 5. It is based on strips of highly reflective rolled sheet metal, which





is clamped to the curved side of a milled base plate. The combined radius of the sheet metal mounted on the base amounts to  $22.58 \text{ mm} \pm 8 \mu\text{m}$ , which was determined with a tactile profilometer. Three holes were punched into the metal strip as orientation markers for easier comparison of different measurements of the same surface region. The topographies are recorded just above the holes punched into the specimen.

### 3.2. Recording and evaluation

After alignment of the specimen in the LSWLI setup, the object is rotated and imaged in incremental steps, which eliminates motion blur. The angular step length of the rotation is adjusted to move the object surface one pixel per frame. This assures the densest correlogram sampling physically possible with this setup without having to resort to sub-pixel sampling. The rotation stage's angular step repeatability is rated at  $3.5 \mu\text{rad}$ . Combined with the specimen's radius and uncertainty this results in a stepping uncertainty of  $0.079 \mu\text{m}$ . The change of the lateral stepsize within the FOV due to the objects curvature follows a cosine-function and is assumed to be negligible for the specimen at angles from  $0^\circ$ – $8^\circ$ , where the change is less than 1 %.

Due to the lateral movement of the surface through the FOV, the correlogram for each surface point is read-out from the recorded stack of images by taking the displacement of the surface per frame into account. This can be implemented in at least two ways, cf figure 6. The surface point's positions in each frame can be directly calculated and addressed, see figure 6(a). The recorded intensities of each point are written sequentially into an array, so that this array contains the surface point's correlogram at the end of the scan. As a lot of read-write operations are needed to copy the correlograms into a secondary matrix, which is used for the correlogram evaluation, this

method is slower than the method presented in figure 6(b). There, the image stack is padded with zeros according to the displacement needed for a surface point to move through the FOV completely. During recording, each frame is correspondingly shifted, so that all intensities from the pixels belonging to a certain surface point appear in the same column of the array. The correlograms can be directly evaluated within this array. This method utilizes less read-write operations, but the padding increases memory demand for larger image stacks. The memory demand can be greatly reduced, if the method is implemented as a buffer, only loading as much images at the same time as are necessary to evaluate one line of correlograms. For this article method B was used, as it promises higher evaluation speeds, which will be important in the long term.

The maximum position of the envelopes of the correlograms are evaluated with Matlab's rms-envelope function with a resolution of one sampling point. The resolution can be increased by upsampling the envelope at the cost of processing time. As processing time and memory space are a limiting factor, upsampling will not be considered in this article.

The time-frequency analysis for Munteanu's method to determine the local signal frequency and the associated local tangent angles is carried out on the correlograms using a continuous wavelet transform with Morse wavelets (CWT) [20]. To obtain the tangent angles  $\Theta(x)$  depending on the surface's principal shape instead of tangent angles of small localized structures (e.g. waviness and roughness), the CWT is applied to a large number of correlograms and the resulting frequencies are then averaged. As a side effect, this reduces the influence of correlogram noise. The final step of the evaluation is the calculation of the structure height from the maxima of the envelopes and the tangent angles using equation (4).

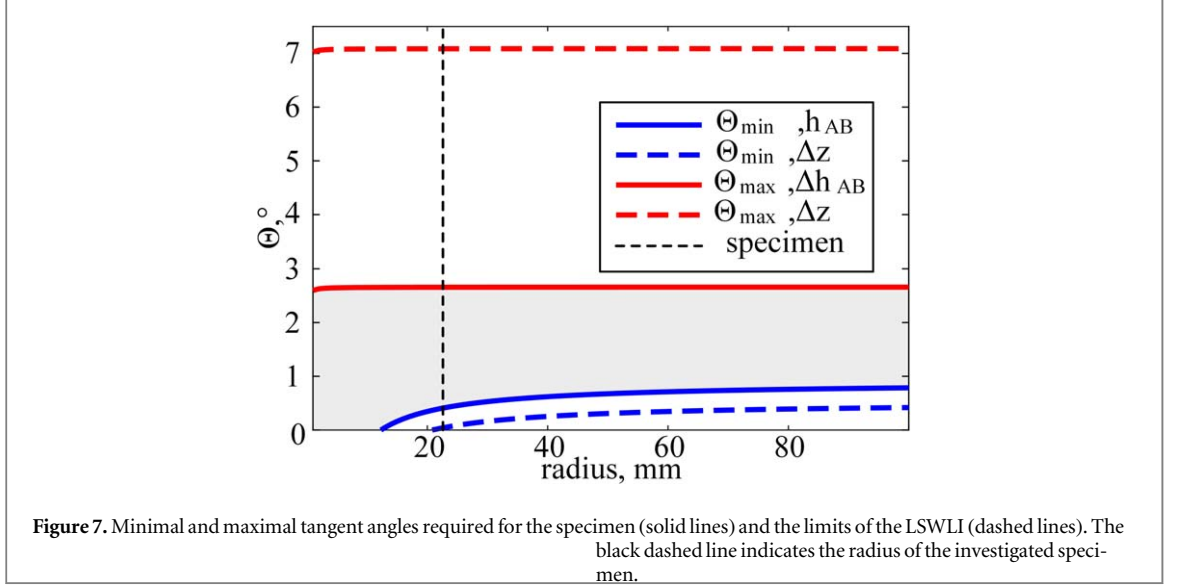


**Table 2.** Measurement positions A-E and their positions with respect to the apex of the specimen.

Measurement	A	B	C	D	E
distance of FOV center to apex [ $\mu\text{m}$ ]	250	450	600	750	1600

### 3.3. Used measurement window

Figure 7 shows the measurement window (grey area) of the experimental setup for different radii, where the setup parameters from section 3.1 are applied to the theoretical findings in section 2.3. The LSWLI-specific upper and lower bounds of the tangent angles according to equations (7) and (9) are shown as dashed lines. For this setup and the specimen radius of 22.6 mm, the lower bound is  $\Theta_{\min, \Delta Z} = 0.07^\circ$  and the upper bound is  $\Theta_{\max, \Delta Z} = 7.09^\circ$ . The minimal and maximal tangent angles required to achieve the measurement range (6  $\mu\text{m}$ ) and resolution (0.1  $\mu\text{m}$ ) according to equations (6) and (8) are shown as solid lines and read for the specimen of 22.6 mm radius at  $\Theta_{\min, h_{AB}} = 0.45^\circ$  and  $\Theta_{\max, \Delta h_{AB}} = 2.66^\circ$ . They lie within the LSWLI-specific limits, so that the desired resolution and measuring range can be achieved with the measurement configuration used.

To investigate the influence of the local tangent angles on the measurement result, the same region of the specimen is measured using five different target angle ranges between  $0.2^\circ$  and  $4^\circ$  (measurement series A-E). This is done by positioning the LSWLI's FOV with respect to the apex (cf figure 4). Changing the FOV's distance to the apex also causes a change in axial distance, which is compensated with manual readjustment, so that the  $z_{\text{OPD}}$ -plane intersects the surface within the FOV. The measurement positions are listed in table 2.

Note that measurement series E ( $\Theta \sim 4^\circ$ ) exceeds the chosen upper, workpiece depending tangent angle limit, in order to test the derived limit equation (equation (8)). So, for series E the measurement range

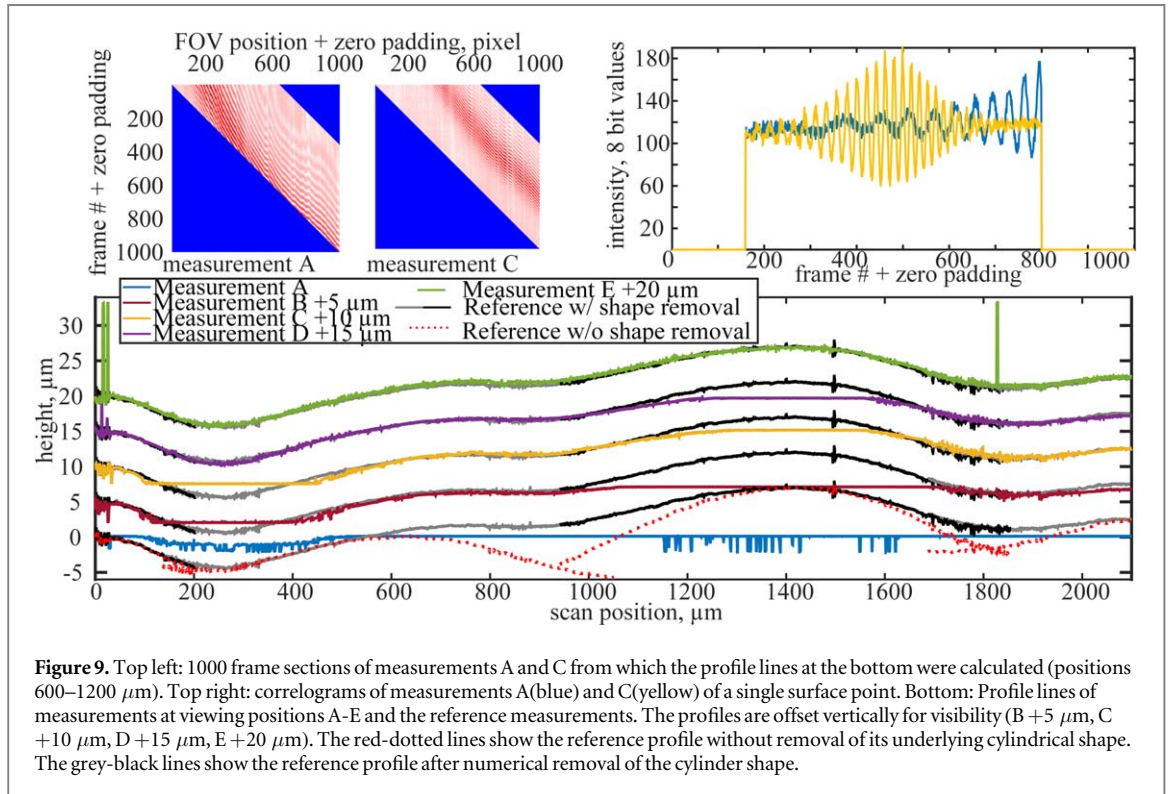
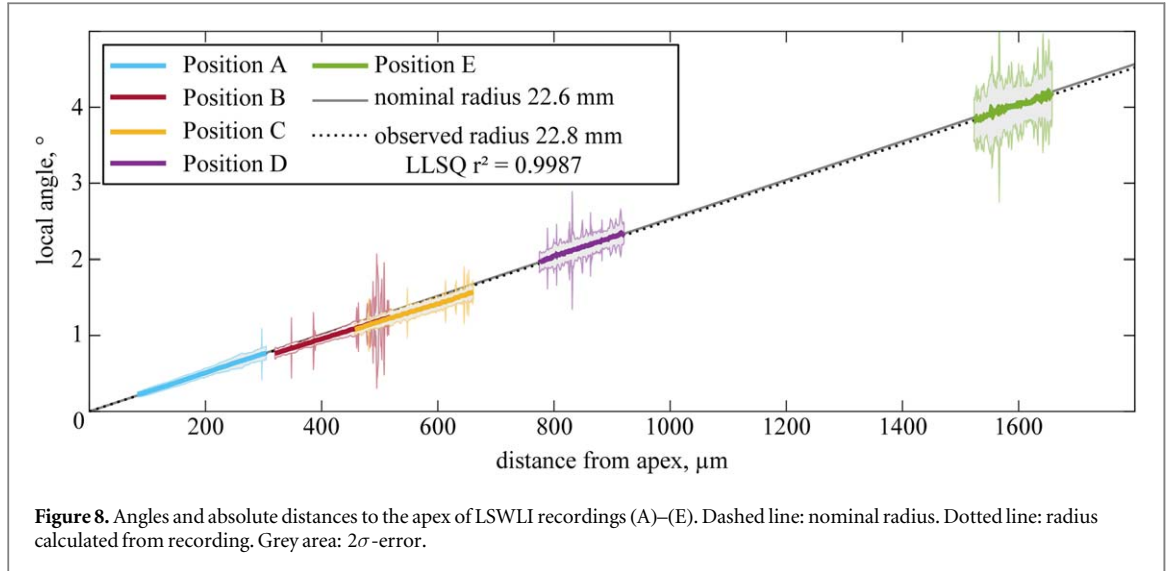
is extended, but the desired physical measurement resolution can no longer be achieved.

## 4. Results and discussion

### 4.1. Angle evaluation

A CWT time-frequency analysis is performed on all LSWLI recordings. Each recording captures the same region of the specimen's surface, but the FOV's distance to the apex is altered and the rotational position of the sample and the distance to the sample are readjusted correspondingly. This results in different observed tangent angles.

To validate the angle evaluation using Munteanu's method in conjunction with time-frequency analysis for use on curved surfaces, the local tangent angles are plotted over the absolute distance of the measurement FOV to the apex in figure 8. The tangent angles are calculated according to equation (5). The angles shown are the mean values of 3300 correlograms per position. The resulting  $2\sigma$ -error of the data is shown as light-grey area. In general, the errors become smaller the closer the measurement position is to the apex. The solid grey line shows the theoretical relationship between tangent angle and apex-distance for the nominal radius of  $r = 22.58$  mm (section 3.1). An approximation of the radius to all measured data (dotted black line) results in a value of  $r = 22.8$  mm (goodness of fit  $R^2 = 0.9987$ ). The radius is calculated using the mean over all positions  $x$  of  $r = x / \sin(\Theta(x))$ . The high goodness of fit is an indicator showing that indeed the same region of the specimen is recorded and that the rotation itself is carried out similarly in each measurement. The deviation of nominal and observed radius is most probably a result of local surface features (e.g. waviness) and eccentric rotation, as a lateral movement of the interference fringes in the FOV is observed during scanning. Radius values are usually approximated from the data of a full rotation of the workpiece. Considering that in this case



only about 2 mm (1.4%) of the total circumference (142 mm) are used to calculate the radius, the result is regarded as plausible and a convenient byproduct of the angle evaluation. Due to these results, the use of Munteanu’s method with time–frequency analysis to evaluate the local tangent angles needed for rotatory LSWLI topographies is considered valid. The obtained linear fits of the angles for each of the measurements A–E are used to calculate the topographies of the recorded regions. The resulting topographies are presented and discussed in section 4.2.

#### 4.2. Topography of the specimen

The topographies resulting from measurements A–E are calculated using the envelope maxima and the

tangent angles of section 4.1. Exemplary sections of the prepared correlograms are shown in the top half of figure 9. The top left shows 1000 shifted frames (see section 3.2) of measurements A and C. A and C are discernible by their different correlogram fringe frequencies, cf top right of figure 9. The small tangent angles set for measurement A caused a much wider interference region than in C. It is in fact wider than the FOV, which results in wrongly evaluated points, as evidenced in the profile lines shown at the bottom of figure 9. A single surface profile of each LSWLI measurement series together with the VSWLI reference data is presented at the bottom of figure 9. The LSWLI profiles are manually aligned horizontally and offset vertically. The shown reference profile line

**Table 3.** Theoretical and actually achieved ranges of the measurements (A)–(E) and their respective physical resolutions.

Measurement	Range, $\mu\text{m}$		Resolutions, nm
	Theoretical	Actual	
A	3.086	2.151	0.83–9.63
B	5.992	5.639	4.85–13.87
C	9.019	8.396	9.62–18.57
D	13.300	12.410	15.98–25.59
E	26.269	24.211	36.31–45.83
Reference	300	12.107	7.1e-4

consists of four single topography measurements, which are manually stitched and shifted to align with the LSWLI measurements.

Three main differences between VSWLI- and LSWLI- recorded topographies can be seen in figure 9.

Firstly, the VSWLI reference measurement originally contains the cylinder shape (dashed red line), which has to be numerically removed using the radius of the specimen. Contrary to the VSWLI measurement, the LSWLI recorded surface topography does not contain the global cylinder shape.

Secondly, looking closely at the reference profile (grey&black solid line) in figure 9, there are stitching artefacts at scan positions 200  $\mu\text{m}$ , 900  $\mu\text{m}$  and 1800  $\mu\text{m}$ , as the reference measurements do not perfectly align with each other. The LSWLI topographies show no such artefacts, as they were recorded during one single measurement scan, which behaves like a development of the cylinder’s shell.

Thirdly, while the VSWLI has a fixed vertical resolution and is limited in range only by the size of the axial scan mechanism, the LSWLI has to compromise between range and resolution, as they are both connected by and depending on FOV-size and angles of the scan path. The five different measurement positions A-E show the influence of the compromise (range versus resolution) on the topography measurement. Measurement series A has the least amount of features, as the measurement range is too low to capture all structures of the specimen. The largest range is present in measurement series E, in which all surface structures are visible and measured without cutting off their peak heights.

While measurement series D records the first valley at scan position 300  $\mu\text{m}$  completely where the series A-C fail, series D’s measurement range is not aligned to capture the hill near scan position 1500  $\mu\text{m}$ , which in turn is captured by series C slightly better.

The physical ranges determined by the sensor size and local tangent angles are compared to the ranges actually present in the five measurements A-E in table 3. Additionally, the range of physical resolution possible in each measurement is shown. Note, that for the reference, the theoretical range is the range of the z-drive and the actual range is assumed to be the height range, that the object possesses.

The achieved ranges of the measurements are smaller than the theoretical ranges for all measurements. This can be explained by considering the actual position of the  $z_{\text{OPD}}$ -plane. If it is not positioned in such a way, that the measured object’s surface intersects the plane everywhere within the FOV, some of the range is lost, e.g. if the interference region never drifts to one edge of the FOV, but exits the FOV at the other edge. If the regions, where the surface intersects with  $z_{\text{OPD}}$  exit the FOV on one side during measurement (cf measurement A at the top of figure 9), this will show up as a plateau, as evidenced in all measurements besides measurement E, which has a range larger than the object’s height range of 12.107  $\mu\text{m}$ , which could have been captured by measurement D completely, if the alignment of  $z_{\text{OPD}}$  had been optimized. The ranges of measurements D and E are in fact larger than the height range present in the reference. This is likely caused by erroneous spikes, like the ones visible at the left edge of the profile lines at the bottom of figure 9. Concerning the range, the bottomline is that due to the nature of the LSWLI method, the operator has to pay special attention when setting up the system for a measurement. Not only is it important to choose an appropriate FOV distance to the apex to achieve the required range, also this available range has to be aligned with the object surface to capture it completely.

The resolutions become coarser with the increasing local tangent angles from A-E. The finer resolution corresponds to the side of the FOV, that is closer to the apex, the coarser resolution to the side away from the apex. The close FOV-side of measurement A actually achieves a sub-nanometer resolution. This is sufficient, considering commercial VSWLIs, like the one used for the reference measurement, apply algorithms that can work with physical resolutions (there it corresponds to the step-height of their z-stage) of  $\lambda_0/8 \approx 66$  nm (using a similar light source). Processing these recordings with advanced interpolation and curve fitting algorithms enables them to achieve sub-nanometer resolutions and uncertainties. This can be satisfied even with measurement E.

Looking at the gradients of the profiles near the ends of their respective measurement ranges, there is a difference between the upper (scan positions between 1000  $\mu\text{m}$  and 1800  $\mu\text{m}$ ) and lower (scan positions between 100  $\mu\text{m}$  and 500  $\mu\text{m}$ ) ends of the ranges: Near the lower ends the profiles become steeper compared to the reference, while they become shallower towards their upper ends. This effect is likely caused by the non-equidistant sampling of heights throughout the FOV. On the FOV end, where the steeper angles are present during measurement, the sampling is not as fine as at the other end. If surface points are associated to the pixels at the steep edge of the FOV by the correlogram evaluation algorithm, they are resolved coarser, causing a step-like appearance. The reverse effect happens at the other edge of the FOV, where sampling



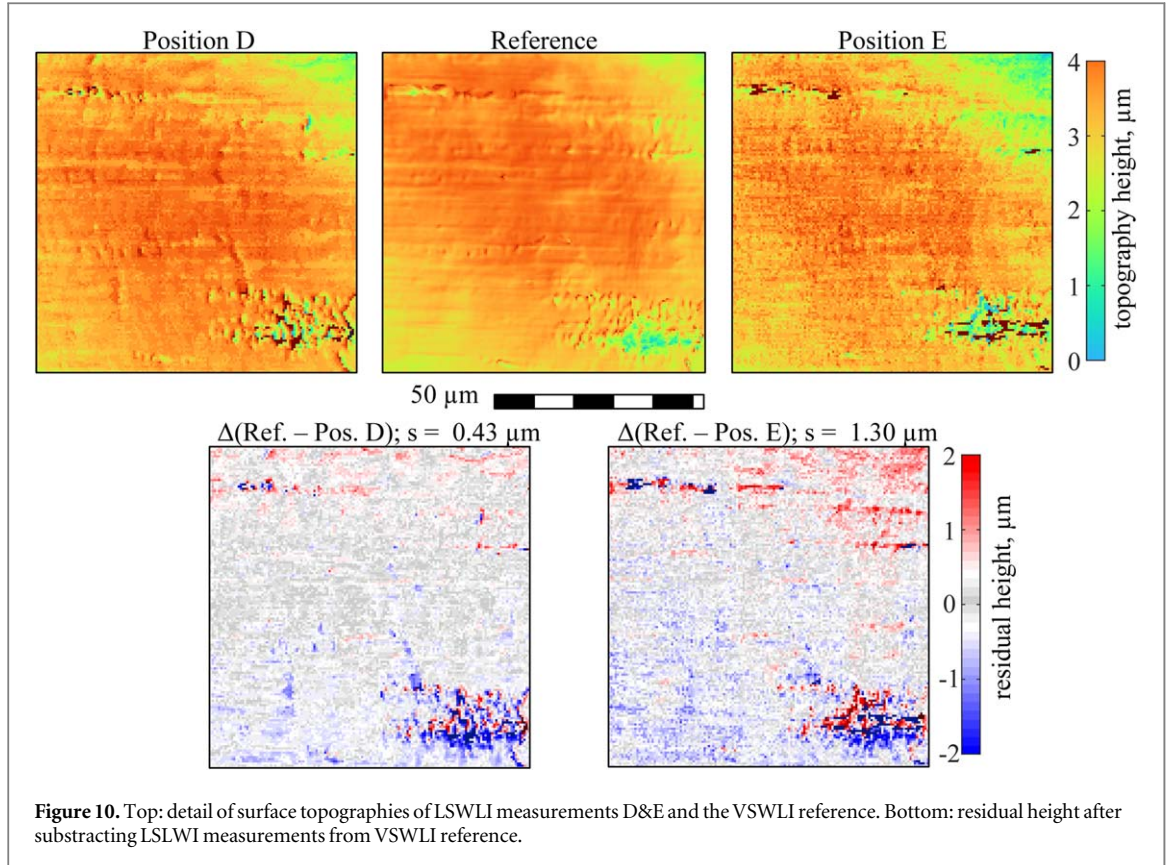


**Figure 10.** Top: detail of surface topographies of LSWLI measurements D&E and the VSWLI reference. Bottom: residual height after subtracting LSWLI measurements from VSWLI reference.

is finer, which in turn causes a shallower gradient between surface points associated to this edge. Besides correctly evaluated points at the edges of the FOV, there are also surface points that are wrongly associated with the edges; these are visible in the figure as spikes. The key takeaways here are that future improvements of the evaluation algorithms should take the non-equidistant sampling into account and that the interference regions should take up a narrower region of the FOV, reducing the chance of false maxima at the edges.

The surface details of measurement series D and E are compared with each other and the VSWLI reference to investigate the influence of the measurement position on the resolution of the topography measurement. The results are shown in figure 10. The scanning direction of the LSWLI measurements is from left to right. The selected area contains several structures specific to sheet metal production such as the horizontal stretching marks and a prominent wrinkled section in the bottom right corner of the detail topographies, both indicating that the rolling direction of the metal was also left to right. Measurement series D was chosen, because it captured the surface topography with the closest resemblance to the VSWLI reference. Series E was chosen, because it constitutes an extreme case regarding the tangent angles present at its measurement position, even surpassing the maximum angle, beyond which the resolution specified in section 3.3 cannot be guaranteed.

While measurement series D yielded a topography, that shows many of the same features visible in

the reference, features are much harder to identify in the measurement series E. Subtracting each LSWLI topography from the reference yields the residual height at the bottom of figure 10. The standard deviations of these residual heights are used to quantify how well the measurements match the reference. Series D ( $s = 0.43 \mu\text{m}$ ) has only about a third of series E's residual's standard deviation ( $s = 1.30 \mu\text{m}$ ). This indicates that the resolution of a LSWLI-sourced topography decreases with increasing distance to the apex (cf figure 8), which is in agreement with the theoretical considerations in section 2.3. The difference in the general spatial resolution of the LSWLI measurements and the reference can be explained with the different hardware between the commercial VSWLI and the experimental-stage LSWLI. As the reference VSWLI has a much larger camera sensor and a  $0.5\times$  tube, it was able to use a  $20\times$  objective while still retaining a lateral resolution finer than that of the experimental LSWLI setup (VSWLI:  $0.48 \mu\text{m}$  versus LSWLI:  $0.58 \mu\text{m}$ ). However, the LSWLI topographies agree well with the VSWLI reference topography and the different LSWLI measurements behave as explained in section 2, so the rotatory LSWLI mode is considered validated.

## 5. Conclusion

The article presents an enhancement of LSWLI to enable topography measurements of rotating cylindrical objects. The realized rotatory LSWLI system is capable



of capturing a surface area of the specimen over a length of 2.1 mm without stitching, which is more than five times the size of a single FOV of the applied camera. As the measurement range and resolution are connected by the tilt angle in LSWLI, a compromise between both has to be made. A comparison between LSWLI measurements on a finely structured specimen with reference measurements with a commercial VSWLI shows that the LSWLI prototype is able to produce plausible results and the derived relationships between measurement range and resolution are validated.

As this article provided a proof of concept for the rotatory LSWLI method, the setup can be upgraded to a higher hardware standard. Using a larger imaging sensor, assuming a similar pixel size as the camera used for this article, allows a larger measurement range while maintaining the measurement resolution without increasing the tangent angles, as the FOV of the WLI becomes larger. The evaluation will greatly benefit from a finer sampling. Even more so, when a memory and processing speed optimized evaluation algorithm with a finer interpolation can be applied, which reduces the chances of falsely evaluating correlograms. Future hardware upgrades should be focused on speed capabilities, as the (in principle infinite) continuous measurement capability of the rotatory LSWLI method is important for in-process and in-line applications. Further investigations on the measurement uncertainty of the measurement system and how each measurement parameter (e.g. illumination or scanning speed) influences it are necessary to optimize this technology for its proposed use.

## Acknowledgments

This work was funded by the German Federal Ministry of Education and Research within the funding program Photonics Research Germany, contract number 13N14696.

The authors would like to thank GBS mbH for providing the reference measurements and CoSynth GmbH & Co. KG for their support in the laboratory.

## ORCID iDs

Gert Behrends  <https://orcid.org/0000-0001-9950-3035>

Dirk Stöbener  <https://orcid.org/0000-0002-1624-2106>

Andreas Fischer  <https://orcid.org/0000-0001-7349-7722>

## References

- [1] Patzelt S, Stöbener D and Fischer A 2019 Laser light source limited uncertainty of speckle-based roughness measurements *Appl. Opt.* **58** 6436–45
- [2] Fischer A and Stöbener D 2019 In-process roughness quality inspection for metal sheet rolling *CIRP Annals - Manufacturing Technology* **68** 523–6
- [3] ISO 1982 Form deviations; Concepts; Classification system, ' in DIN 4760:1982-06, DIN (<https://doi.org/10.31030/1110827>)
- [4] ISO 2013 Geometrical product specifications (GPS) - Surface texture: Areal - Part 604: Nominal characteristics of non contact (coherence scanning interferometry) instruments, ' in DIN EN ISO 25178-604, ISO (<https://doi.org/10.31030/1968179>)
- [5] Flournoy P A, McClure R and Wytjies G 1972 White-light interferometric thickness gauge *Appl. Opt.* **11** 1907–15
- [6] Davidson M, Kaufman K, Mazor I and Cohen F 1987 An application of interference microscopy to integrated circuit inspection and metrology *Proc. SPIE 0775 Integrated Circuit Metrology, Inspection, & Process Control (Santa Clara, CA, United States)* (<https://doi.org/10.1117/12.940433>)
- [7] Lee B S and Strand T C 1990 Profilometry with a coherence scanning microscope *Appl. Opt.* **29** 3784–8
- [8] Kino G and Chim S 1990 Mirau correlation microscope *Appl. Opt.* **29** 3775–83
- [9] de Groot P 2015 Principles of interference microscopy for the measurement of surface topography *Adv. Opt. Photon.* **7** 1–65
- [10] Wyant J C 2002 White light interferometry *Holography: A Tribute to Yuri Denisjuk and Emmett Leith Proc. SPIE 4737* pp 98–107
- [11] Lehmann P 2010 Vertical scanning white-light interference microscopy on curved microstructures *Opt. Lett.* **35** 1768–70
- [12] Riebeling J, Lehmann P, Laubach S and Ehret G 2017 Combination of a fast white-light interferometer with a phase shifting interferometric line sensor for form measurements of precision components *59th Ilmenau Scientific Coll.* [urn:nbn:de:gbv:ilm1-2017iwk-059-7](https://nbn-resolving.org/urn:nbn:de:gbv:ilm1-2017iwk-059-7)
- [13] Su R, Wang Y, Coupland J and Leach R 2017 On tilt and curvature dependent errors and the calibration of coherence scanning interferometry *Opt. Express* **25m** 3297–310
- [14] Scheiding S, Yi A Y, Gebhardt A, Li L, Risse S, Eberhardt R and Tünnermann A 2011 Freeform manufacturing of a microoptical lens array on a steep curved substrate by use of a voice coil fast servo tool *Opt. Express* **19** 23938–51
- [15] Olszak A 2000 Lateral scanning white-light interferometer *Appl. Opt.* **39** 3906–13
- [16] Munteanu F 2010 Self-calibrating lateral scanning white-light interferometer *Appl. Opt.* **49** 2371–5
- [17] Bahr S, Otto M-A, Domaschke T and Schüppstuhl T 2017 Continuous digitalization of rotationally symmetrical components with a lateral scanning white light interferometer *Tagungsband des 2. Kongresses Montage Handhabung Industrieroboter* ([https://doi.org/10.1007/978-3-662-54441-9\\_14](https://doi.org/10.1007/978-3-662-54441-9_14))
- [18] Domaschke T, Schüppstuhl T and Otto M 2014 Robot guided white light interferometry for crack inspection on airplane engine components *Conf. ISR Robotic*
- [19] Lehmann P, Tereschenko S and Xie W 2016 Fundamental aspects of resolution and precision in vertical scanning white-light interferometry *Surface Topography: Metrology and Properties* **4** 024004
- [20] Lilly J M and Olhede S C 2012 General Morse wavelets as a superfamily of analytic wavelets *IEEE Trans. Signal Process.* **60** 6036–41